J. Fluid Mech. (1973), *vol.* 59, *part* 3, *pp.* 593–620
Printed in Great Britain

Viscous flow over a cone at moderate incidence. Part 2. Supersonic boundary layer

By T. C. LIN AND S. G. RUBIN

Polytechnic Institute of Brooklyn, Preston R. Bassett Research Laboratory, Farmingdale, New York

(Received 18 September 1972 and in revised form 15 March 1973)

A finite-difference method recently developed to study three-dimensional viscous flow is applied here to the supersonic boundary layer on a sharp cone at moderate angles of incidence ($\alpha/\theta \leqslant 2$, angle of attack α, cone half-angle θ). The present analysis differs from previous investigations of this region in that (i) boundary-layer similarity is not assumed, (ii) the system of governing equations incorporates lateral diffusion and centrifugal force effects, and (iii) an improved numerical scheme for three-dimensional viscous flows of the type considered here is used. Solutions are shown to be non-similar at the separation streamline with local shear-layer formation. Detailed flow structure, including surface heat transfer, boundary-layer profiles and thickness, and the formation of swirling pairwise symmetric vortices, associated with cross-flow separation, are obtained. Good agreement is obtained between the present theoretical results and the existing experimental data.

1. Introduction

The high-speed flow over a sharp cone at incidence represents a three-dimensional fluid dynamic problem encompassing a wide variety of phenomena that have recently been observed experimentally, but for which analytic treatment is to date incomplete. With the availability of the latest generation of high-speed computers, inviscid calculations by Moretti (1967) and Jones (1968), among others, have led to significant improvement of previous approximate theories. However, if experimentally observed behaviour is to be confirmed analytically, the influence of viscosity on the flow field must be evaluated.

The flow field on a cone exhibits shock–boundary-layer merging, near the tip, until the strong interaction region where a coupled but distinct inner boundary layer and outer shock wave develop. Analysis in these regions is quite complex, and at the present the only available solutions are the merged or single-layer calculations of the authors presented in part 1 of this analysis (Lin & Rubin 1972). It has been shown that, even at moderate angles of incidence ($\alpha/\theta \leqslant 2$), (i) conical flow pressure is recovered very close to the tip on the windward surface, but only further downstream on the leeward plane; (ii) the heat transfer adjusts to its asymptotic values less rapidly; (iii) the leeward plane inviscid vortical singularity diffuses into a thin entropy layer, and a 'lift-off' effect occurs for $\alpha/\theta > 1$;

(iv) cross-flow separation does not originate close to the cone tip. This result confirms the experimental observations of Stetson (1972).

Further downstream the coupling between the boundary layer and inviscid flow is diminished, and a three-dimensional boundary-layer problem must be formulated. The outer pressure distribution can be obtained from either inviscid analysis (e.g. Jones 1968), single-layer analysis (Lin & Rubin 1972) or experiment (e.g. Tracy 1963).

Moore (1953) was the first to examine the boundary-layer behaviour along the symmetry planes on a slender cone at incidence. He assumed parabolic similarity of the boundary layer and a conical inviscid flow. Although results for the windward plane were acceptable, Moore was able to obtain leeward plane solutions only for very small angles of incidence. He reasoned that at large incidence the leeside boundary layer must depend on the history of the fluid during its passage around the cone. Since the symmetry plane equations are independent of the out-of-plane flow, no such influence was considered. Other symmetry plane analyses have also resulted in the non-uniqueness or non-existence of leeward, and sometimes even windward, plane solutions (Murdock 1971; Roux 1971; Cheng 1961; Trella & Libby 1965).

Cooke (1966), McGowan & Davis (1970), Boericke (1971) and Roux (1971) solved the simplified quasi-two-dimensional similarity boundary-layer equations by integrating around the cone, starting at the windward surface, where the entire flow must be predetermined. However, they were still unable to obtain solutions at the lee surface except for very small angles of yaw. Significantly, this integration in the azimuthal (ϕ) direction represents an initial-value problem of a first-order (in ϕ) differential equation, so that one can never be sure that the leeward plane symmetry conditions, and in particular the approach to zero cross-flow, will be satisfied. McGowan & Davis (1970) formulated a general procedure for three-dimensional boundary layers, patterned on the numerical method developed by Krause, Hirschel & Bothmann (1969). However, cross-flow diffusion was not considered, and the numerical method is only marginally stable for negative cross-flows. Also, for spinning and non-circular cones, an initial plane solution on the windward surface is not readily obtainable, so that these methods becomes less desirable (Dwyer 1971).

Moreover, it was shown by Boericke (1971) that the simplified equations at the leeward side of the cone exhibit behaviour typical of either a node or a saddle point, and are therefore extremely difficult to treat by numerical means. In addition, for $\alpha/\theta \geqslant 1$, the cross-flow may exceed sonic speeds near $\phi = \frac{1}{2}\pi$, and then must decelerate through a sonic point back to zero velocity as the leeside of the cone is approached. This results in a mixed type of partial differential equation, and adds yet another difficulty. Finally, when secondary-flow separation occurs ($\alpha/\theta > 0{\cdot}8$), reverse cross-flow velocities are encountered, and the azimuthal marching technique becomes unstable.

The aforementioned analyses all assume a constant pressure boundary layer, conical outer flow conditions, similarity for the boundary layer, and negligible crosswise diffusion. At the leeward plane, for small angle of incidence, and off the leeward plane for large yaw angles, these approximations become suspect.

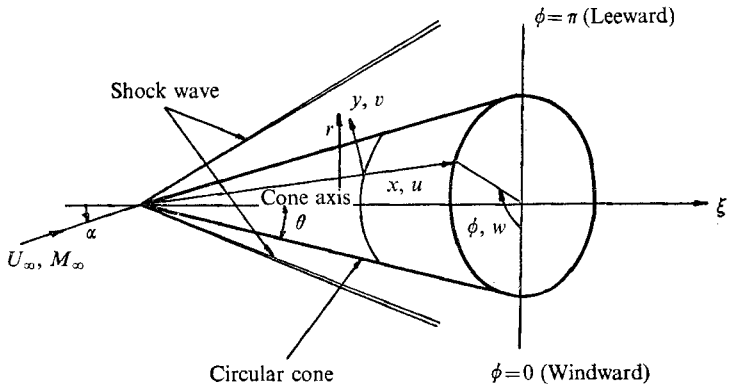

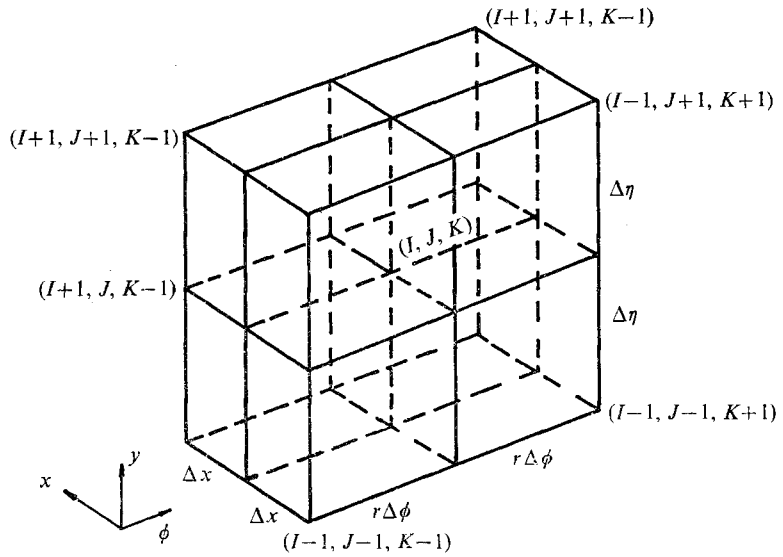

FIGURE 1. Flow geometry and numerical grid.

In the present paper, the laminar flow over a slender cone at moderate angles of incidence (i.e. $\alpha/\theta \leqslant 2{\cdot}0$) is studied analytically with a numerical finite-difference technique recently developed by the authors for general three co-ordinate viscous flow problems. We intend to develop an efficient numerical scheme to determine all three-dimensional flow properties on a cone at incidence, including the first analytic determination of secondary-flow separation, the formation or roll-up of spiral vortices, and the flow structure at the location of the separation streamlines (e.g. the leeward plane at small incidence).

The primary differences between this approach and the above analyses are as follows. (i) An initial-value problem is formulated in the streamwise direction only, and parabolic boundary-layer similarity is not postulated. If a similar solution does exist, it will be obtained asymptotically. (ii) A starting streamwise plane solution for the cross-flow integration is no longer necessary. (iii) The

governing equations presented here are modified so as to include the effects of centrifugal forces due to large cross-flow velocities, as well as lateral diffusion near cross-flow separation planes. The validity of the usual three-dimensional boundary-layer equations is carefully and critically examined. (iv) The finite-difference scheme applied here was developed by the authors specifically for three-dimensional viscous flow studies.

In § 2 the governing equations are presented. The boundary conditions, initial profiles, and numerical finite-difference method are discussed in §§ 3, 4 and 5, respectively. Details of the numerical solutions for the flow structure, including comparisons with available experimental data, the effects of grid size, surface temperature and Mach number are discussed in § 6. Finally, there is in § 7 a summary of the most significant results and conclusions.

2. The governing equations

A body-fixed co-ordinate frame $(\bar{x}, \bar{y}, \bar{\phi})$ with velocities $\bar{u}$, $\bar{v}$, $\bar{w}$, respectively, is defined in figure 1, where $\bar{r}$ is the cylindrical co-ordinate measured from axis of symmetry, i.e.

$$\bar{r} = \bar{x}\sin\theta + \bar{y}\cos\theta.$$

The following non-dimensionalization and change of variable is prescribed:

$$u = \bar{u}/\bar{U}_\infty, \quad v = \bar{v}[Re\,x]^{\frac{1}{2}}\exp\{-\beta\bar{\phi}\}/\bar{U}_\infty, \quad w = \bar{w}/\bar{U}_\infty\sin\alpha,$$
$$p = \bar{p}/\bar{p}_\infty, \quad T = \bar{T}/\bar{T}_\infty, \quad \rho = \bar{\rho}/\bar{\rho}_\infty,$$
$$x = \bar{x}/L, \quad r = \bar{r}/L, \quad \eta = \bar{y}\,Re^{\frac{1}{2}}x^{-\frac{1}{2}}\exp\{-\beta\phi\}/L,$$
$$\phi = \bar{\phi}, \quad \mu = \bar{\mu}/\bar{\mu}_\infty, \quad Re = \bar{\rho}_\infty\bar{U}_\infty L/\bar{\mu}_\infty.$$

α is the angle of attack, β is a prescribed function of α/θ; since no characteristic length is present for this analysis, L is chosen as 1 in. or 1 ft, depending on the Reynolds number of the flow being considered.

The three-dimensional boundary-layer equations in the transformed plane, modified to include centrifugal force and cross-flow diffusion effects, become:

continuity,

$$x(\rho u)_x - \frac{\eta}{2}(\rho u)_\eta + (\rho v)_\eta + \frac{x}{r}[\sin\alpha(\rho w)_\phi - \beta\eta\sin\alpha(\rho w)_\eta + \rho u\sin\theta + \rho v(Re\,x)^{-\frac{1}{2}}\exp\{\beta\phi\}\cos\theta] = 0; \tag{2.1a}$$

x momentum,

$$x\rho u u_x - \frac{\eta}{2}\rho u u_\eta + \rho v u_\eta + \frac{\rho w\sin\alpha}{r}x(u_\phi - \beta\eta u_\eta) - \frac{x}{r}\rho w^2\sin^2\alpha\sin\theta + \frac{x}{M_\infty^2\gamma}p_x - \exp\{-2\beta\phi\}(\mu_\eta u_\eta + \mu u_{\eta\eta}) - \exp\{-\beta\phi\}\left(\frac{x}{Re}\right)^{\frac{1}{2}}\frac{\mu}{r}\cos\theta u_\eta = \epsilon\frac{x}{r^2}\frac{1}{Re}\{u_\phi[\mu_\phi - \beta\eta\mu_\eta] - \beta\eta\mu_\phi u_\eta + \beta^2\eta^2\mu_\eta u_\eta + \beta^2\mu\eta^2 u_{\eta\eta} + \mu\beta^2\eta u_\eta - 2\mu\beta\eta u_{\eta\phi} + \mu u_{\phi\phi}\}; \tag{2.1b}$$

y momentum,

$$p_\eta = \epsilon M_\infty^2\gamma(\sin^2\alpha)\,x^{\frac{1}{2}}\exp\{\beta\phi\}(Re)^{-\frac{1}{2}}\frac{\rho w^2\cos\theta}{r}; \tag{2.1c}$$

ϕ momentum,

$$\rho u x w_x - \frac{\rho u}{2}\eta w_\eta + \rho v w_\eta + \frac{\rho w \sin\alpha}{r} x[w_\phi - \beta\eta w_\eta]$$
$$+\frac{\rho u w}{r} x\sin\theta + \frac{x}{r M_\infty^2 \gamma \sin\alpha}(p_\phi - \beta\eta p_\eta \epsilon) - \exp\{-2\beta\phi\}(\mu_\eta w_\eta + \mu w_{\eta\eta})$$
$$-\frac{\mu}{r}\cos\theta\left(\frac{x}{Re}\right)^{\frac{1}{2}}\exp\{-\beta\phi\}w_\eta = \epsilon\frac{4}{3}\frac{x}{Re}\left\{\frac{\mu}{r^2}[\beta^2\eta^2 w_{\eta\eta} + \beta^2\eta w_\eta - 2\beta\eta w_{\eta\phi} + w_{\phi\phi}]\right.$$
$$\left.+\frac{1}{r^2}[\mu_\phi w_\phi - \beta\eta\mu_\eta w_\phi - \beta\eta\mu_\phi w_\eta + \beta^2\eta^2\mu_\eta w_\eta]\right\}; \tag{2.1d}$$

energy,

$$\rho u x T_x - \frac{\rho u}{2}\eta T_\eta + \rho v T_\eta + \frac{\rho w \sin\alpha x}{r}[T_\phi - \beta\eta T_\eta]$$
$$+p(\gamma-1)x\left[u_x - \frac{1}{2}\frac{\eta}{x}u_\eta + \frac{v_\eta}{x} + \frac{\exp\{\beta\phi\}v\cos\theta\, Re^{-\frac{1}{2}}x^{-\frac{1}{2}}}{r}\right.$$
$$\left.+\frac{u\sin\theta}{r} + \frac{\sin\alpha}{r}(w_\phi - \beta\eta w_\eta)\right] - \frac{\gamma}{Pr}\left[\exp\{-2\beta\phi\}(\mu_\eta T_\eta + \mu T_{\eta\eta})\right.$$
$$\left.+\frac{\mu}{r}\left(\frac{x}{Re}\right)^{\frac{1}{2}}\exp\{-\beta\phi\}\cos\theta T_\eta\right] - M_\infty^2\gamma(\gamma-1)\exp\{-2\beta\phi\}[\mu u_\eta^2 + \mu\sin^2\alpha w_\eta^2]$$
$$= \epsilon\left\{\frac{\gamma}{Pr}\frac{x}{Re}\frac{1}{r^2}[\mu_\phi T_\phi - \beta\eta\mu_\eta T_\phi - \beta\eta\mu_\phi T_\eta + \mu_r\beta^2\eta^2 T_\eta^2 + \mu\beta^2\eta^2 T_{\eta\eta} + \beta^2\eta\mu T_\eta\right.$$
$$-2\beta\eta\mu T_{\eta\phi} + \mu T_{\phi\phi}] + \frac{x}{Re}M_\infty^2\gamma(\gamma-1)\frac{\mu}{r^2}[u_\phi^2 - 2\beta\eta u_\phi u_\eta + \beta^2\eta^2 u_\eta^2$$
$$\left.+\tfrac{4}{3}\sin^2\alpha(w_\phi^2 - 2\beta\eta w_\phi w_\eta + \beta^2\eta^2 w_\eta^2) + \sin^2\alpha\cos\theta w^2]\right\}; \tag{2.1e}$$

state,

$$p = \rho T \quad (r = x\sin\theta + \eta\cos\theta(Re/x)^{-\frac{1}{2}}\exp\{\beta\phi\}). \tag{2.1f}$$

Here, if $\epsilon = 0$, the familiar three-dimensional boundary-layer equations with transverse curvature effects are recovered; when $\epsilon = 1$, lateral diffusion as typified by $u_{\phi\phi}$, etc., as well as centrifugal force effects are retained in the governing equations.

Our basic system (2.1) is deduced from the Navier–Stokes equations under the fundamental assumption that viscous regions will be confined to a thin layer near the wall, so that the Reynolds number $Re = \bar{\rho}_\infty \bar{U}_\infty L/\bar{\mu}_\infty \gg 1$. As is usually the case in boundary-layer analysis, streamwise diffusion is a higher-order effect, so that terms such as $\bar{u}_{\bar{x}\bar{x}}$ and $\bar{T}_{\bar{x}\bar{x}}$ have been neglected. However, crosswise diffusion has not been neglected ($\epsilon = 1$), and, as will be shown later, these terms are significant near the separation streamline, i.e. at the lee side for small incidence and off the leeward plane for moderate angles of yaw. Without the cross-flow diffusion terms (e.g. $u_{\phi\phi}$, $w_{\phi\phi}$) a singularity would be encountered at the separation line. Here we implicitly assume that the cone is infinitely long so that no upstream influence from the cone-base region is possible. The set of equations

(2.1) is not restricted to small or subsonic cross-flow, and parabolic similarity for the boundary layer has not been prescribed.

3. The boundary conditions

The boundary conditions at the cone surface are, with no slip,

$$y = 0,\ u = v = w = 0,\ T = T_w \text{ (isothermal wall)},\ T_y = 0 \text{ (adiabatic wall)}, \quad (3.1)$$

and at the symmetry plane, $\phi = 0$ or π, $y > 0$, w is antisymmetric with

$$u_\phi = T_\phi = \rho_\phi = p_\phi = 0.$$

The conditions at the outer edge of the boundary layer can generally be obtained from solutions of the inviscid Euler equations. The inviscid conical flow calculations of Moretti (1967), Jones (1968), or results obtained from the method of characteristics, are all in reasonable agreement for $\alpha/\theta \leqslant 1{\cdot}0$. For larger yaw angles these inviscid analyses are no longer adequate, as local viscous–inviscid interaction, disappearance of the leeward plane outer shock wave or movement of the lee side vortical singularities introduce additional complications. In lieu of these solutions the existing experimental data of, e.g., Tracy (1963), Rainbird (1968) and Yahalom (1971), or the strong interaction solutions† of Lin & Rubin (1972), are available to test the theoretical model and numerical formulation. The only required input data for the present calculation is the surface pressure and this can be obtained from any of the sources described above. For most of the results to be discussed later, experimental pressure values were prescribed. The pressure distribution is suitably curve fitted to assure the smoothness of the profile, i.e.

$$\bar{p}_w/\bar{p}_\infty = \sum_{n=0}^{m} a_n \cos n\phi. \quad (3.2)$$

The number of terms chosen in the Fourier expansion (3.2) is dependent on the specific angle of attack (e.g. $m = 5$, at $\alpha = 4^\circ$ and $m = 10$ for $\alpha = 20^\circ$). When additional terms are included in the series (3.2), the effects on the numerical solutions are minimal.

With the conical flow assumption for the outer inviscid region, the Euler equations at the cone surface become

$$\left.\begin{aligned} u_\phi &= w \sin\theta \sin\alpha, \\ w w_\phi \sin^2\alpha + u w \sin\alpha \sin\theta &= -\frac{1}{\rho M_\infty^2 \gamma} p_\phi, \\ T = 1 + \frac{\gamma-1}{2} M_\infty^2 - \frac{\gamma-1}{2} M_\infty^2 (u^2 + w^2 \sin^2\alpha), \\ p &= \rho T. \end{aligned}\right\} \quad (3.3)$$

In view of the split symmetry conditions, $w = 0$ at $\phi = 0$ and π, an eigenvalue problem for the unknown velocity $u_e(0)$ at the windward plane results. For the

† The surface pressure achieves asymptotic conical conditions close to the cone tip.

smaller angles of yaw, $\alpha < 10°$, a trial-and-error implicit shooting method, with integration from the windward to the leeward side of the cone, is combined with a Newton–Raphson iteration procedure in order to determine the value of $u_e(0)$ that leads to a zero cross-flow velocity at the leeward plane. This unidirectional shooting, from $\phi = 0$ to π, is not applicable for larger angles of attack, as the mathematical nature of the leeward plane singular point changes character. This can be seen by solving for w_ϕ from (3.3), whereby

$$w_\phi = -\frac{u\sin\theta}{2\sin\alpha} \pm \frac{\sin\theta}{2\sin\alpha}\sqrt{D},$$

and

$$D = u^2 - \frac{4p_{\phi\phi}}{\rho M_\infty^2 \gamma \sin^2\theta}. \tag{3.4}$$

Therefore, we find that, at the symmetry planes where $w = p_\phi = 0$, the differential equation (3.4) exhibits (i) a stable node for $D < 0$, $p_{\phi\phi} > 0$; (ii) a stable focus for $D < 0$, $p_{\phi\phi} > 0$; and (iii) a saddle point for $D > 0$, $p_{\phi\phi} < 0$ (Hales 1969). With a free-stream Mach number $M_\infty = 8$, a cone half-angle $\theta = 10°$, and the inviscid pressure results of Jones (1968), we find from (3.4) that the windward plane exhibits a saddle point behaviour for all angles of incidence. At the leeward generator, case (i) applies for $\alpha \leqslant 2°$; case (ii) for $4° \leqslant \alpha < 8°$; and case (iii) for $\alpha > 10°$.

With the unidirectional shooting method and $\alpha < 10°$, the iteration procedure for the eigenvalue $u_e(0)$ converges rapidly. For $\alpha \geqslant 10°$, a saddle point is encountered at the leeward plane and a process of double shooting is required. Solutions from the windward and leeward planes are matched at some prescribed intermediate points until the velocities differed by less than a set tolerance, usually 10^{-3} (see figure 2). The exact matching position is not known *a priori* but results from the iteration procedure. These techniques proved to be extremely satisfactory for obtaining the outer inviscid values at all angles of incidence $\alpha \leqslant 20°$, $\theta_c = 10°$. For $\alpha/\theta \leqslant 1{\cdot}1$, Jones (1968) has presented detailed solutions which are compared with the present values on figure 2(*b*) and table 1. The results generally agree to within 1 % for $\alpha = 7°$ and 10 % for $\alpha = 11°$. In view of the curve fitting procedure adopted here for the pressure and Jones's extrapolation procedure for the surface values, which is somewhat inaccurate for the larger angle, the agreement is quite reasonable. For $\alpha > 11°$, Jones was not able to obtain solutions, and even for $\alpha = 11°$ his surface distribution is not very smooth (figure 2(*b*)).

The vorticity at the outer edge of the boundary layer, in particular at the leeward plane, is assumed to vanish so that any vorticity interaction would be a higher-order effect. Lin & Rubin (1972) have shown that in the tip region the vorticity singularity diffuses within the boundary layer into a vortical region and also that the concept of 'lift-off' of the entropy layer is possible in a viscous flow (see also Yahalom 1971). In this case, one would not expect a significant vorticity interaction near the edge of the boundary layer. If the inviscid singularity remains outside, but near the edge of the boundary layer, vorticity effects might be important. These have not been considered here.

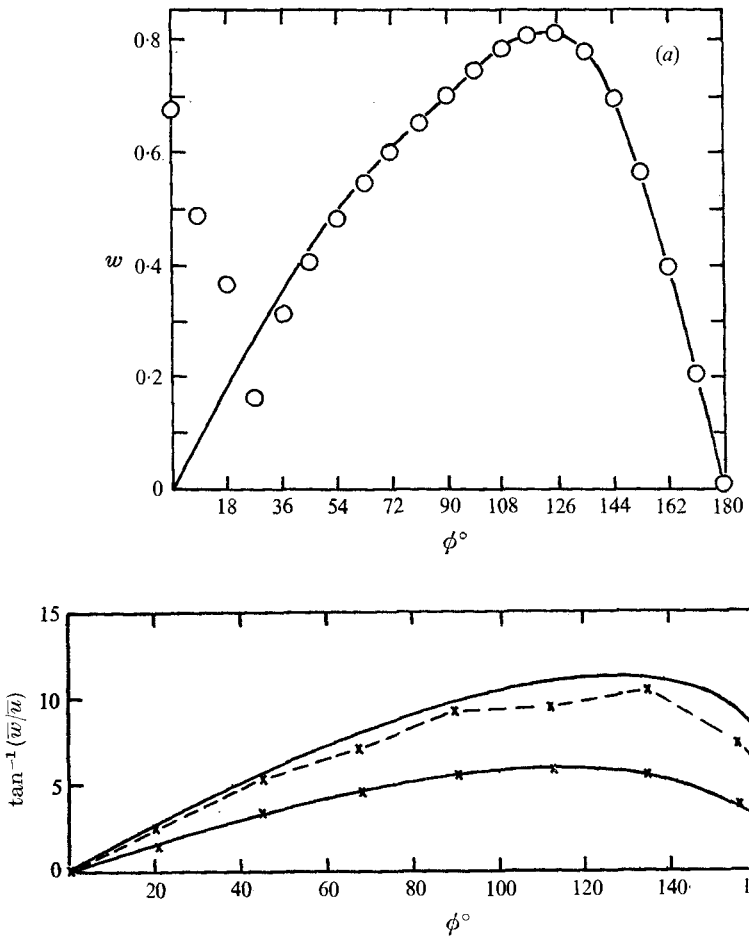

FIGURE 2. (*a*) Inviscid cross-flow inclination. $M_\infty = 7{\cdot}95, \theta = 10°, \alpha = 12°$. ○, leeward plane to windward plane; ——, windward plane to leeward plane. (*b*) Inviscid streamline. $M_\infty = 10{\cdot}0, \theta = 10°, \alpha = 11°$ (above), 7° (below). ×, inviscid surface conditions (Jones 1968); ——, present theory.

		ϕ							
$\tan^{-1}(\bar{w}/\bar{u})$	0	22·5	45	67·5	90	112·5	135	157·5	180
		(*a*) $\alpha = 7°, M_\infty = 10, \theta = 10°$							
Jones	0	1·732	3·284	4·583	5·517	5·851	5·384	3·502	0
Present method	0	1·726	3·291	4·601	5·533	5·870	5·390	3·471	0·000
		(*b*) $\alpha = 11°, M_\infty = 10, \theta = 10°$							
Jones	0	2·667	5·333	7·017	9·217	9·300	10·300	7·239	0
Present method	0	2·830	5·701	7·889	9·650	10·619	11·090	8·050	0·000

TABLE 1. Inviscid streamline inclination (degrees)

In certain experiments the appearance of weak embedded shocks has been reported for the largest incidence considered here $\alpha/\theta \approx 2$ (e.g. Tracy 1963; Yahalom 1971), although other experimental data (e.g. Stetson 1972) have not confirmed such formation. If an embedded shock does form when $\alpha/\theta \leqslant 2$, it is extremely weak, and in fact cannot be detected by vapour screen techniques or with a schlieren optical system (Yahalom 1971). Surface pressure measurements are also inconclusive. For larger incidence $\theta = 5°$, $\alpha = 24°$ or $\alpha/\theta > 4$ vapour screen, and schlieren photographs obtained by Feldhun (1971) showed the appearance of stronger internal shocks. At the angles of incidence considered here, such effects will be minimal at most, and therefore have not been considered explicitly. Of course, for the larger angles of incidence considered here, the experimental pressure distribution is applied so that the effect of even a weak internal shock is considered implicitly.

4. Initial conditions

The flow profiles as obtained from the merged and strong interaction results of Lin & Rubin (1972) represent one possible mechanism for generating initial profiles for the present cone boundary-layer calculations. However, several alternative methods for representing the initial conditions have been tested and will now be described.

(i) *Self-generated profiles.* At the initial station, the body geometry as well as the boundary conditions at the edge of the boundary layer and at the wall are known. A set of profiles for u, w and T can be assumed that satisfies all the necessary boundary conditions. Improved values are then calculated by marching one step in the streamwise direction with the finite-difference scheme of § 5. The surface and outer boundary values are held fixed. New initial profiles are then assigned to the initial station by taking the average of the previously assumed and newly calculated values. By repeating this process, the solutions quickly converge until the difference between two consecutive iterations is less than a prescribed tolerance which is set equal to Δx. This technique for generating the initial conditions relies on the same computer program as for the subsequent marching process and is simple to apply.

(ii) *Experimental data.* If available.

(iii) *Arbitrary initial profiles.* Since the governing equations (2.1) are parabolic, the error associated with incorrect initial values will rapidly decay. For the present, three-dimensional boundary-layer calculations, a linear distribution for the streamwise velocity u, a Poiseuille flow distribution for the cross-flow w and the use of a Crocco temperature–velocity relationship were tested. It should be noted that the initial profiles for v are not specified, but rather calculated from the known values of u, T and w. Here an iterative scheme, first suggested by Krause (1967), is employed,† in order that v be determined to any prescribed order of accuracy.

† Here v is evaluated at the mid-station $I + \frac{1}{2}$ (figure 1) in lieu of Krause's averaged I and $I + 1$ values.

At a distance of $0{\cdot}3L$ from the starting location, the heat transfer, as obtained from the various initial values, are almost indistinguishable (Lin & Rubin 1972).

5. Numerical finite-difference scheme

The numerical finite-difference scheme used here is a predictor and corrector semi-implicit method. The details of the representation of the difference quotients, inversion of matrices, the stability and consistency analysis of the predictor–corrector method and further discussion concerning the effects of nonlinearity and iteration are presented in Rubin & Lin (1971, 1972) and Rubin (1972).

6. Results

In § 6 a detailed study of the surface conditions and boundary-layer profiles on cones at angles of incidence up to twice the cone half-angle is presented. Complete solutions, from the windward to the leeward plane, including cross-flow separation and vortex formation are discussed. Many of the results presented herein represent the first analytic determination of these complex three-dimensional phenomena.

The majority of the numerical results presented here are obtained at conditions corresponding to the experiments of Tracy (1963) and George (1969): $M_\infty = 7{\cdot}95$; $Re\,\mathrm{in}^{-1} = 1{\cdot}1 \times 10^5$; $\bar{T}_0 = 1360^\circ R$; $T_w/T_0 = 0{\cdot}41$; $\theta = 10^\circ$; $\gamma = 1{\cdot}4$. In addition, the effects of Mach number and surface temperature are also discussed. Unless stated otherwise the calculations always include the effect of lateral diffusion (i.e. $\epsilon = 1$ in (2.1)). The Sutherland viscosity law is applied throughout the computation. Typical run times are from 10 to 40 minutes on a CDC 6600 computer, depending on the extent of the grid, the angle of incidence and the final streamwise distance.†

6.1. *Flow patterns*

The general flow structure for $\alpha/\theta \leqslant 2{\cdot}0$ as obtained from the present calculations will now be discussed. In particular, results relating to cross-flow separation, vortex formation and surface or limiting streamline patterns within the entire separation region, which to the authors' knowledge have been obtained analytically for the first time, are presented. The influence of these phenomena on surface heat transfer, boundary-layer thickness and flow properties in general are briefly outlined, with a more complete analysis presented in §§ 6.2–6.4.

With modern oil-film techniques surface streamline traces can be readily detected. For cone flows these provide a good method for describing the overall flow behaviour. The direction of a local limiting streamline is defined by

$$\theta_w = \tan^{-1}\frac{\bar{w}}{\bar{u}}\bigg|_{\bar{y}=0} = \tan^{-1}\frac{\bar{w}_{\bar{y}}}{\bar{u}_{\bar{y}}}\bigg|_{\bar{y}=0}.$$

Figure 3 depicts the θ_w distribution from the windward to the leeward plane for different incidence angles. Also shown are the experimental traces of McDevitt

† Most of the calculations are based on the experimental pressure distribution.

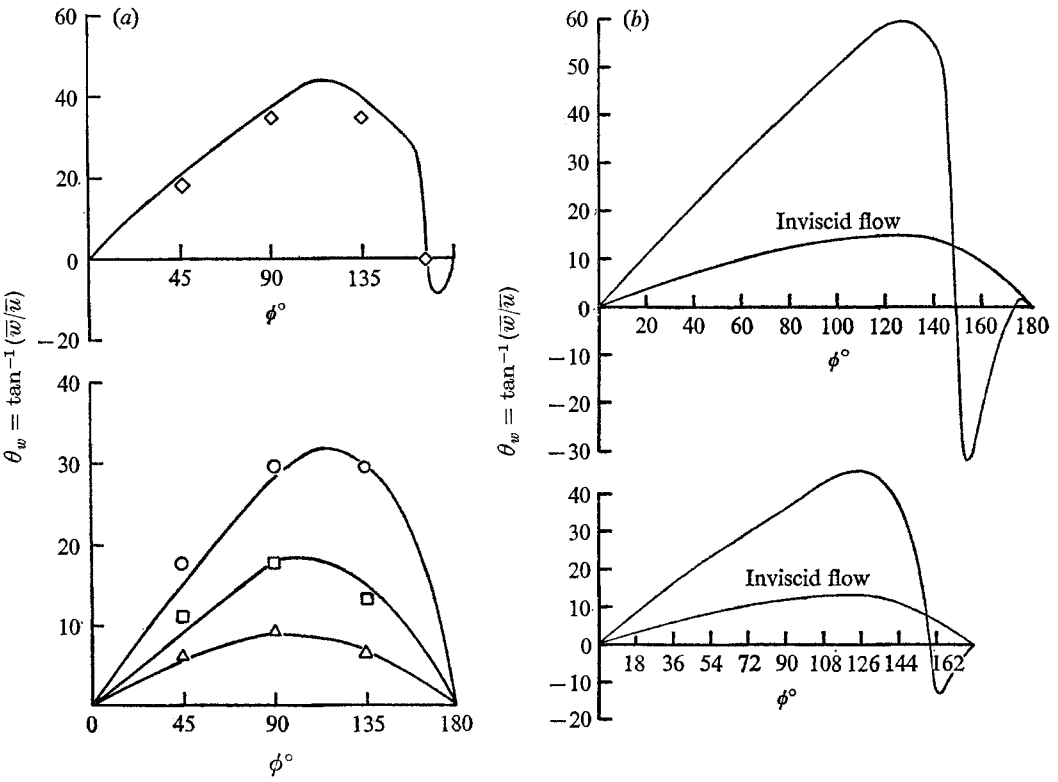

FIGURE 3. Surface streamline inclination. $M_\infty = 7{\cdot}95$, $\theta = 10°$; $T_w/T_0 = 0{\cdot}41$. (*a*) Experimental data; oilfilm (McDevitt & Mellenthin 1969): △, $\alpha = 2°$; □, 4°; ○, 8°; ◇, 10°. ——, present theory; $Re = 1{\cdot}04 \times 10^5$ in.$^{-1}$; $\bar{x} = 3{\cdot}0$ in. (*b*) $\alpha = 20°$ (above), 12° (below). $Re\, x = 2{\cdot}1 \times 10^5$.

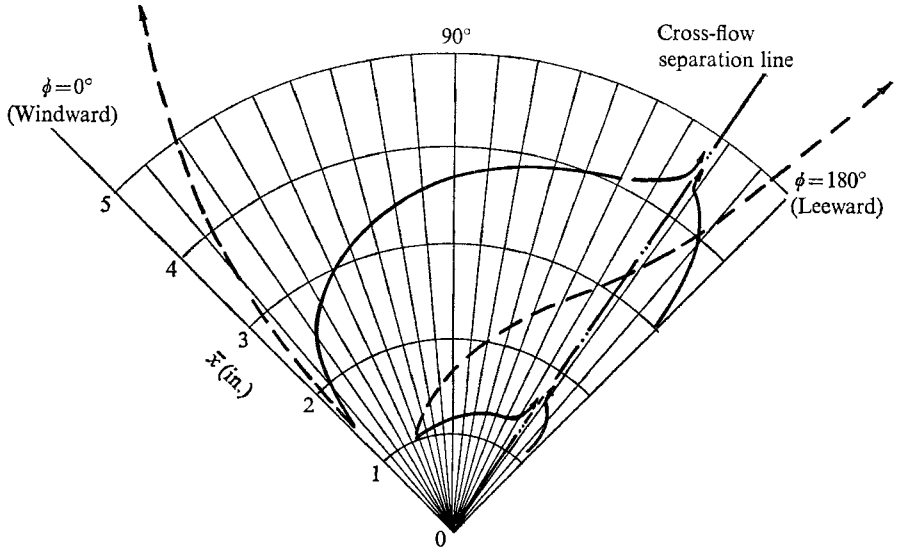

FIGURE 4. Surface streamline patterns. $M_\infty = 7{\cdot}95$, $\theta = 10°$, $\alpha = 12°$, $T_w/T_0 = 0{\cdot}41$. ——, surface; – – –, inviscid streamline projections.

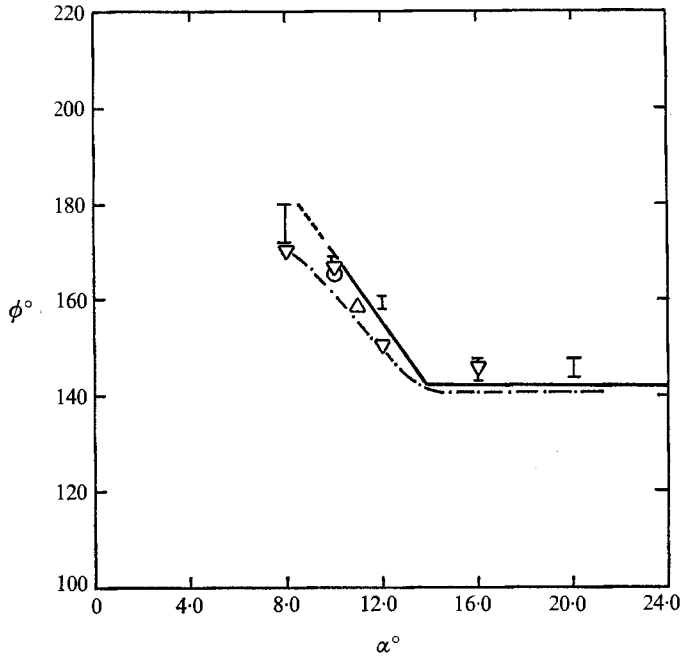

FIGURE 5. Cross-flow separation point. $M_\infty \approx 4, \ldots, 10$, $\theta = 10°$. Experimental data: ——, Avduevskii & Medvedev (1966); △, Tracy (1963); ○, McDevitt & Mellenthin (1969); ▽, George (1969); —·—, Marcillat (1970). I, present theory.

& Mellenthin (1969). As the streamwise variation in θ_w is small in the weak interaction region, we will assume that $\theta_w = \theta_w(\phi)$. By integrating the surface streamline equation

$$\frac{\bar{r}\, d\phi}{d\bar{x}} = \theta_w(\phi) \quad \text{at} \quad \bar{y} = 0,$$

the shapes of the limiting streamlines have been determined. Some results are depicted on figure 4. Also shown are the surface projections of the outer inviscid streamlines. One feature of cross-flow separation is the appearance of an inflexion point locus in the surface flow pattern as depicted on figure 4. From figures 3 and 4 we observe that the largest streamline deflexion due to the significant cross-flow velocity is of the order of 45° at $\alpha = 12°$ and up to 60° for $\alpha = 20°$. The surface streamlines can be as much as 50° out of phase with their free-stream values. The fluid particles closest to the wall undergo their largest change of direction near the cross-flow separation line, the location of which is shown on figure 5. The experimental observations of Avduevskii & Medvedev (1966) and McDevitt & Mellenthin (1969) are also presented. The agreement is good and generally within the experimental error.†

To understand further the flow structure of these complex three-dimensional

† The spread in the theory reflects variations due to the choice of pressure distribution or streamwise location.

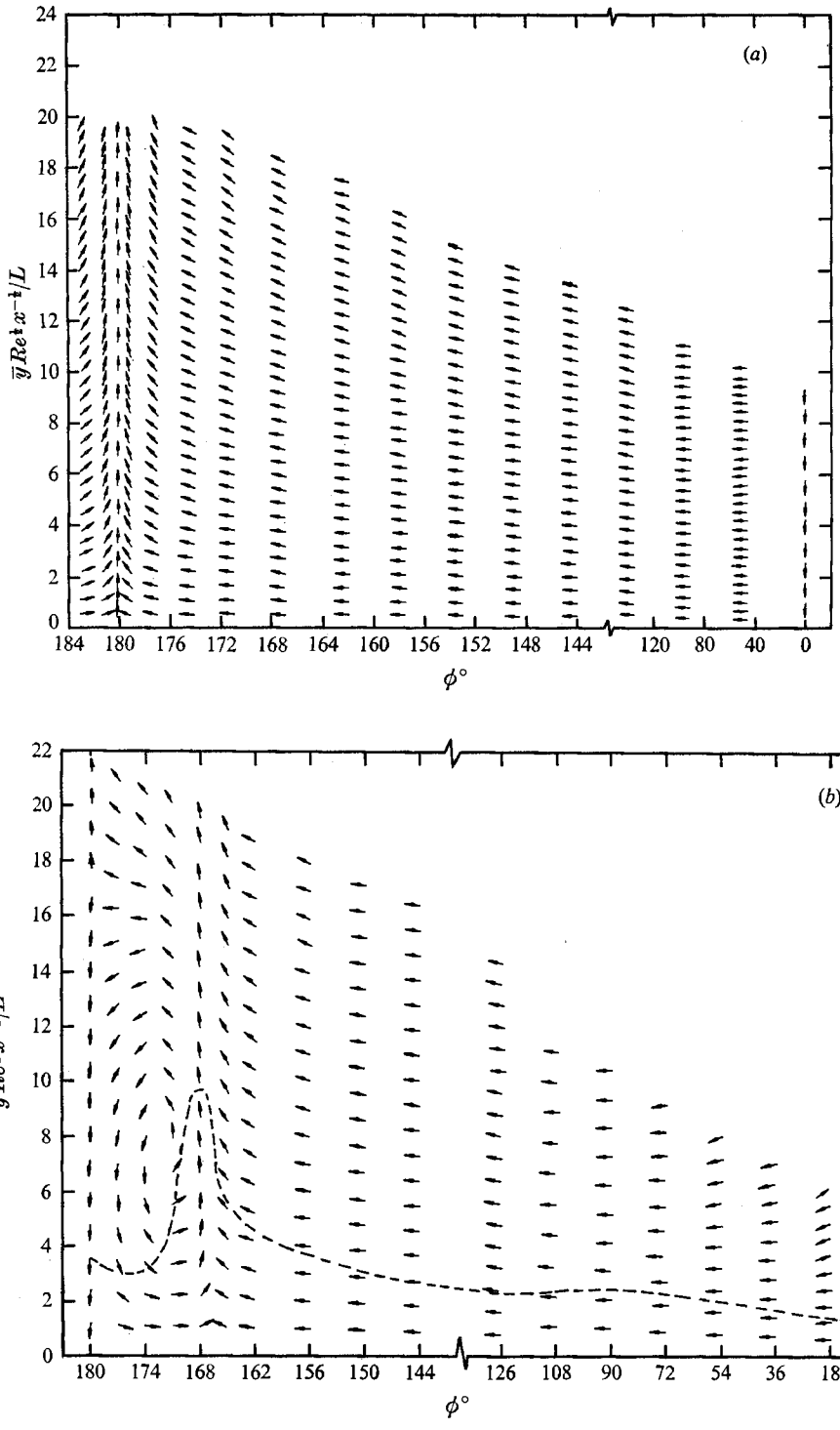

FIGURES 6(*a*) and (*b*). For legend see following page.

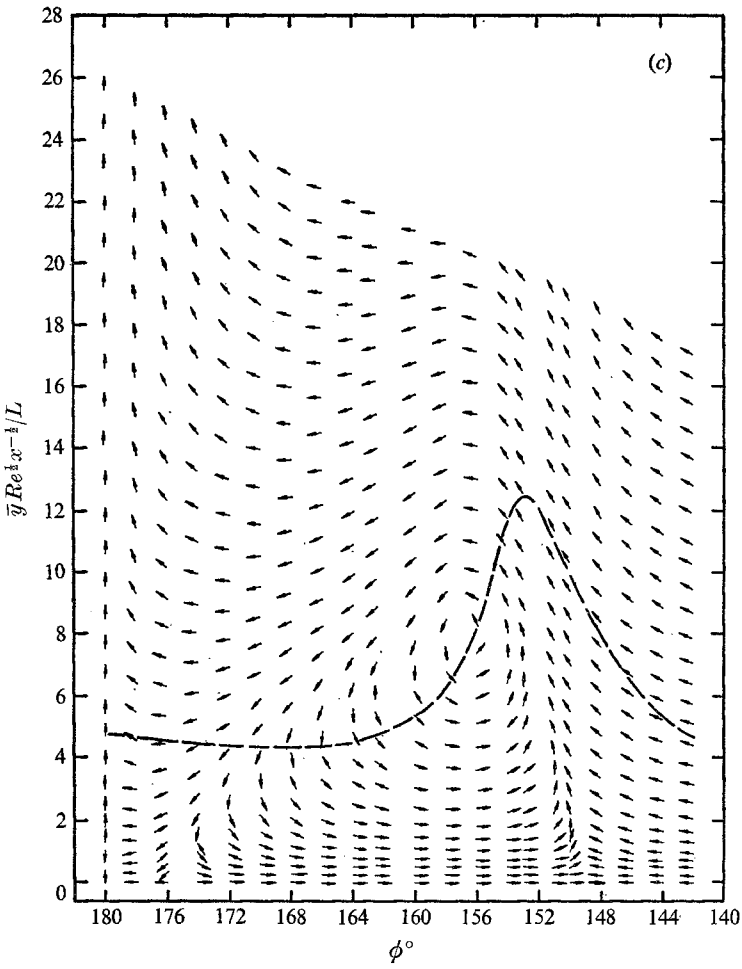

FIGURE 6. Projected stream surfaces. $M_\infty = 7{\cdot}95$, $\theta = 10°$, $T_w/T_0 = 0{\cdot}41$. ---, sonic line; $(\bar{u}^2+\bar{w}^2)^{\frac{1}{2}}/\bar{a} = 1$. (*a*) $Re\,x = 3{\cdot}6 \times 10^5, \alpha = 8°$. (*b*) $Re\,x = 3{\cdot}6 \times 10^5, \alpha = 10°$. (*c*) $Re\,x = 2{\cdot}1 \times 10^5$, $\alpha = 20°$.

boundary layers, the local flow inclinations Θ in the y, ϕ plane, corresponding to streamline projections on the cross-plane, are shown:

$$\Theta = \tan^{-1}\frac{\bar{v}}{\bar{w}}\bigg|_{\bar{x}}.$$

These are illustrated in figures 6 for $\alpha = 8$, 10 and 20°, respectively. In the latter two cases secondary-flow reversal associated with adverse azimuthal pressure gradients occurs near the leeside of the cone. From the figure it is seen that vortex sheets originate from the cone surface, at the primary separation line, then roll up to form a pair of symmetric swirling vortices. These vortex sheets are composed of fluid from both the lower surface boundary layer and the outer higher velocity edge region of the boundary layer. The mixing process brings the

high-energy fluid downward and toward the leeside, while carrying the low-energy fluid away from the plane of symmetry. This transfer process leads to the appearance of a local maximum in the heat transfer at $\phi = 180°$. This type of vortex-induced, intense localized heating in the vicinity of the leeside has also been found experimentally on a space shuttle vehicle and delta wing configuration (Whitehead & Bertram 1971). When this cross-flow vortex is considered with the overall streamwise motion, a pair of symmetric helical vortices can be visualized.

The local sonic line positions, where $M = [(\bar{u}^2+\bar{w}^2)/\gamma RT]^{\frac{1}{2}} = 1$, are also indicated in figure 6. The major portion of the vortex is moving at supersonic speeds and, as certain experiments have indicated, may explain why there is little communication between the boundary layer on a finite length cone and its base flow.

A very interesting result is the appearance of secondary vortices near the lee plane in the $\alpha = 20°$ case. From figure 3 (*b*) we can see that at $176° \leqslant \phi \leqslant 180°$ cross-flow reversal occurs for a second time as the vortex structure becomes more complex. The secondary vortices, although quite small, will alter the nature of the boundary layer at the leeward plane. Secondary vortex formation has been observed experimentally (e.g. Rainbird 1968). More detailed studies of the flow near the lee plane at large angles of incidence will have to be made before these results can be considered conclusive. For the present cone considerations, the separation phenomena that occurs is primarily one of cross-flow reversal. It should be classified of the free vortex layer type (Maskell 1955).

Finally, an interesting feature of flow separation on cones at small incidence, $\alpha \leqslant 8°$, is observed. At these incidence angles there is neither cross-flow reversal nor any appearance of swirling vortices; however, streamlines converge at the leeward plane, which forms a separation surface dividing the flow emanating from the windward attachment plane. From figure 6 (*a*) we see that the flow pattern in the y, ϕ cross-plane is similar to a 'reversed stagnation point' flow; here, of course, streamwise convection plays an important role, and alters the character of the flow structure, as will be seen in the following discussion.

In summary, we find that vortices are initiated in response to an adverse azimuthal pressure gradient developing from opposing cross-flows. The vortices are maintained entirely within the boundary layer. As the vortex interacts with the established boundary layer, high localized heat transfer and the thinning of boundary layer at the symmetry plane results. For favourable azimuthal gradients ($\alpha < 8°$), vortex formation does not occur.

6.2. *Pitot pressure and boundary-layer thickness*

Pitot pressure distributions, within the boundary layer, at a constant height above the cone surface are presented in figure 7. When the local Mach number is subsonic, an isentropic deceleration is assumed. Agreement between the theoretical predictions and Tracy's (1963) experimental results is only fair. At $\alpha = 4°$ (not shown) and 8° (figure 7 (*a*)), a rapid drop in pitot pressure near the leeward generator is observed. This would indicate that in the vicinity of the

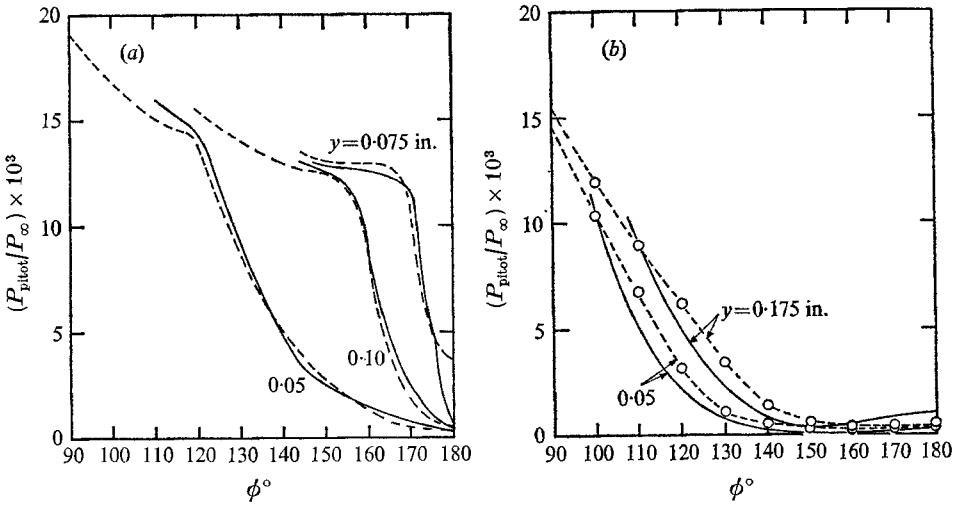

FIGURE 7. Pitot pressure profiles. $M_\infty = 7{\cdot}95$, $\bar{x} = 3{\cdot}45$ in.; $T_w/T_0 = 0{\cdot}41$, $Re\,x = 3{\cdot}6 \times 10^5$. ---, experimental data (Tracy 1963); ——, present theory. (*a*) $\alpha = 8°$, (*b*) 20°.

lee plane, the lateral derivative should be quite large, possibly of the same order as the normal or $\bar{y}$ derivative, i.e.

$$\frac{1}{\bar{x}}\frac{\partial}{\partial\phi} = O\left(\frac{\partial}{\partial\bar{y}}\right).$$

On the other hand, the pitot data near the wall show little variation in the azimuthal direction with $\alpha = 20°$ (figure 7(*b*)). Here the largest variation in pitot pressure around the cone occurs in the inviscid flow region.

Figure 8(*a*) depicts the variation of the symmetry plane boundary-layer thickness δ with streamwise distance x. Typical parabolic growth is indicated for all angles of incidence on the windward plane. This surface corresponds to an attachment line, in that the normal velocity component is always directed toward the body. The leeward plane in the same sense corresponds to either an attachment or separation line. For $\alpha/\theta < 0{\cdot}8$, cross-flow separation is not observed, but there is an accumulation of low-energy fluid into the leeward generator. Therefore, the boundary-layer thickness is largest along this line. Moreover, for angles of incidence less than 2°, the profiles are 'similar' with respect to the Blasius boundary-layer co-ordinate, even with a non-zero cross-flow velocity and streamline convergence into the leeward meridian. Therefore, with $\alpha \leqslant 2°$, on both symmetry planes, $\delta \sim x^{\frac{1}{2}}$.

For $2° \leqslant \alpha \leqslant 8°$, the leeward plane no longer behaves as a typical Blasius boundary layer. In these cases, secondary flows are significantly increased. The rate of mass accumulation into the lee side is so large that the boundary layer has to grow more rapidly to accommodate the influx. Surprisingly, our calculated results show that for $\alpha = 4°$, the surface heat transfer C_H still retains an $x^{-\frac{1}{2}}$ or similarity-like dependence; the local boundary-layer thickness is not similar, however, but grows more rapidly; i.e. $\delta \sim x^{0{\cdot}8}$ (figure 9). These results are in agreement with all experimental data, and seem to indicate that the viscous-

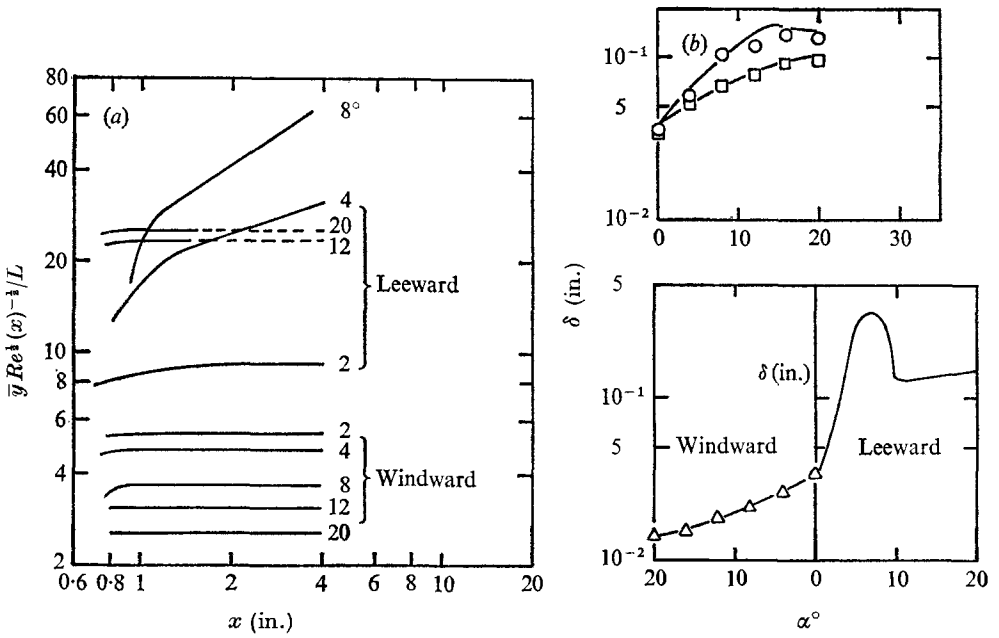

FIGURE 8. Symmetry plane boundary-layer growth. $M_\infty = 7{\cdot}95$, $T_w/T_0 = 0{\cdot}41$. (*a*) Streamwise variation. $Re = 1{\cdot}04 \times 10^5\,\text{in.}^{-1}$ (*b*) Variation with α. $Re\,x = 3{\cdot}6 \times 10^5$, $\bar{x} = 3{\cdot}45$ in. △, similarity results (Reshotko 1957); ○ ($\phi = 150°$), □ (130), experimental data (Tracy 1963); ——, present theory.

dominated region near the body surface still exhibits a similarity type of behaviour, with the outer portion of the boundary layer accommodating the incoming mass flux.

At still larger incidence angles, $\alpha \geqslant 10°$, the leeside boundary-layer thickness returns to a near similar parabolic form.† Cross-flow separation has occurred, and the non-similar region moves away from the leeward meridian to a new separation line.

It is significant that at angles of attack between 2° and 8°, where our solutions indicate that the flow is not similar at the lee plane, the parameter

$$K = 2\bar{w}_{e\phi}/(3\bar{u}_e \sin\theta),$$

evaluated at the leeward plane, is in the range $-0{\cdot}67 < K < -0{\cdot}08$. This is precisely the region where leeward plane similarity solutions have failed to exist (Murdock 1971). When $\alpha > 8°$, the boundary layer at the leeward generator returns to a parabolic growth, so that it is possible to obtain meaningful results with Moore's (1953) similarity model; indeed, Murdock has obtained solutions for $-1{\cdot}0 \leqslant K \leqslant -0{\cdot}67$. This clearly demonstrates that one of the reasons for the non-existence of lee plane solutions at certain angles of incidence is due to the assumption of parabolic similarity. In a subsequent discussion, we shall also point out the significance of lateral diffusion in the symmetry plane analysis.

† There is still small but non-zero streamwise variation in the flow properties at and near the leeward boundary layer.

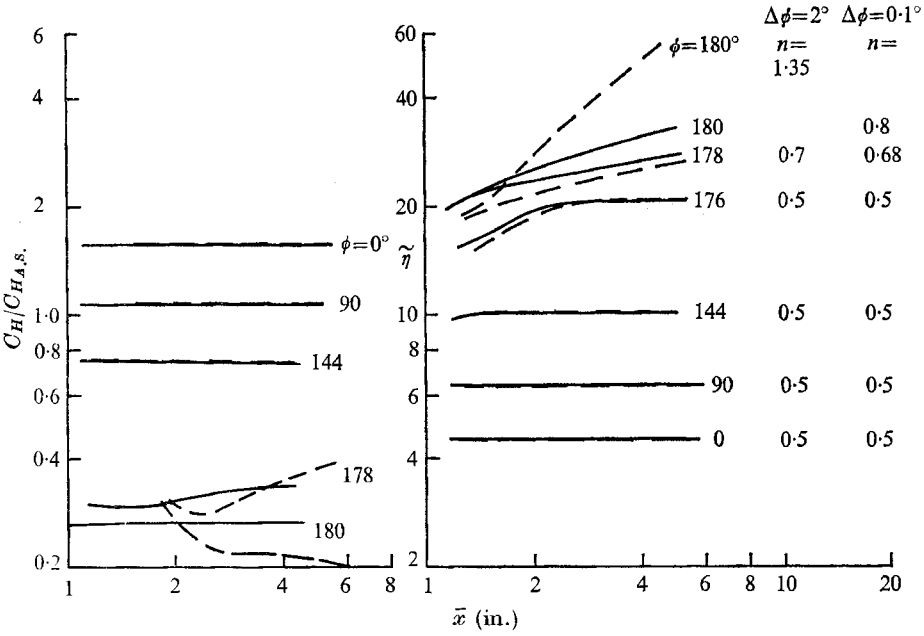

FIGURE 9. Boundary-layer thickness and C_H. $M_\infty = 7{\cdot}95$, $\theta = 10°$, $\delta \sim x^n$, $\alpha = 4°$. ---, $\Delta\phi_{\min} = 2°$; ——, 0·1. $\eta = \delta/x^{\frac{1}{2}}$; $\tilde{\eta} = \bar{y}\,Re^{\frac{1}{2}}x^{-\frac{1}{2}}/L \sim \eta$.

The distribution of δ in the ϕ direction is shown in figure 10(*a*). Good agreement is found with Tracy's viscous-layer thickness, except at the lee plane, where our results indicate a larger value of δ for $\alpha = 4°$ and 8°. For $\alpha = 4°$–8°, δ/r_w is less than 0·1, except near the lee plane, where $\delta/r_w \approx 0{\cdot}4$. Therefore, a second-order boundary-layer correction may be important in this region. Figure 10(*b*) depicts the displacement thickness Δ for $\alpha = 8°$ and 20°. The displacement thickness, which has been derived by Moore (1951) and Lighthill (1958), is defined by

$$\sin\theta\frac{\partial}{\partial x}[\rho_e u_e x(\Delta-\delta_x)]+\frac{\partial}{\partial\phi}[\rho_e w_e(\Delta-\delta_\phi)] = 0,$$

where $$\delta_x = c_1\int_0^\infty (1-\rho u/\rho_e u_e)\,d\eta, \quad \delta_\phi = c_1\int_0^\infty (1-\rho w/\rho_e w_e)\,d\eta,$$

and $$c_1 = \exp\{\beta\phi\}\,x^{\frac{1}{2}}(\rho_\infty U_\infty L/\mu_\infty)^{-\frac{1}{2}}.$$

A modified Simpson's rule is used to evaluate the integrals, i.e.

$$\int_{(N-1)\Delta\eta}^{N\Delta\eta} F\,d\eta = \frac{\Delta\eta}{12}[5F_{N-1}+8F_N-F_{N+1}].$$

It is apparent from figure 10(*b*) that δ_x closely approximates Δ, even at $\alpha = 20°$ when the cross-flow is definitely not small.

Our numerical results also indicate that at a given streamwise location δ (or Δ) is largest near the cross-flow separation line. With $\alpha \leqslant 8°$ this position is located at the lee side, but gradually moves to $\phi = 145°$ for $\alpha = 20°$. The location of this separation line is illustrated in figure 5. For the larger incidence angles $\alpha \geqslant 10°$,

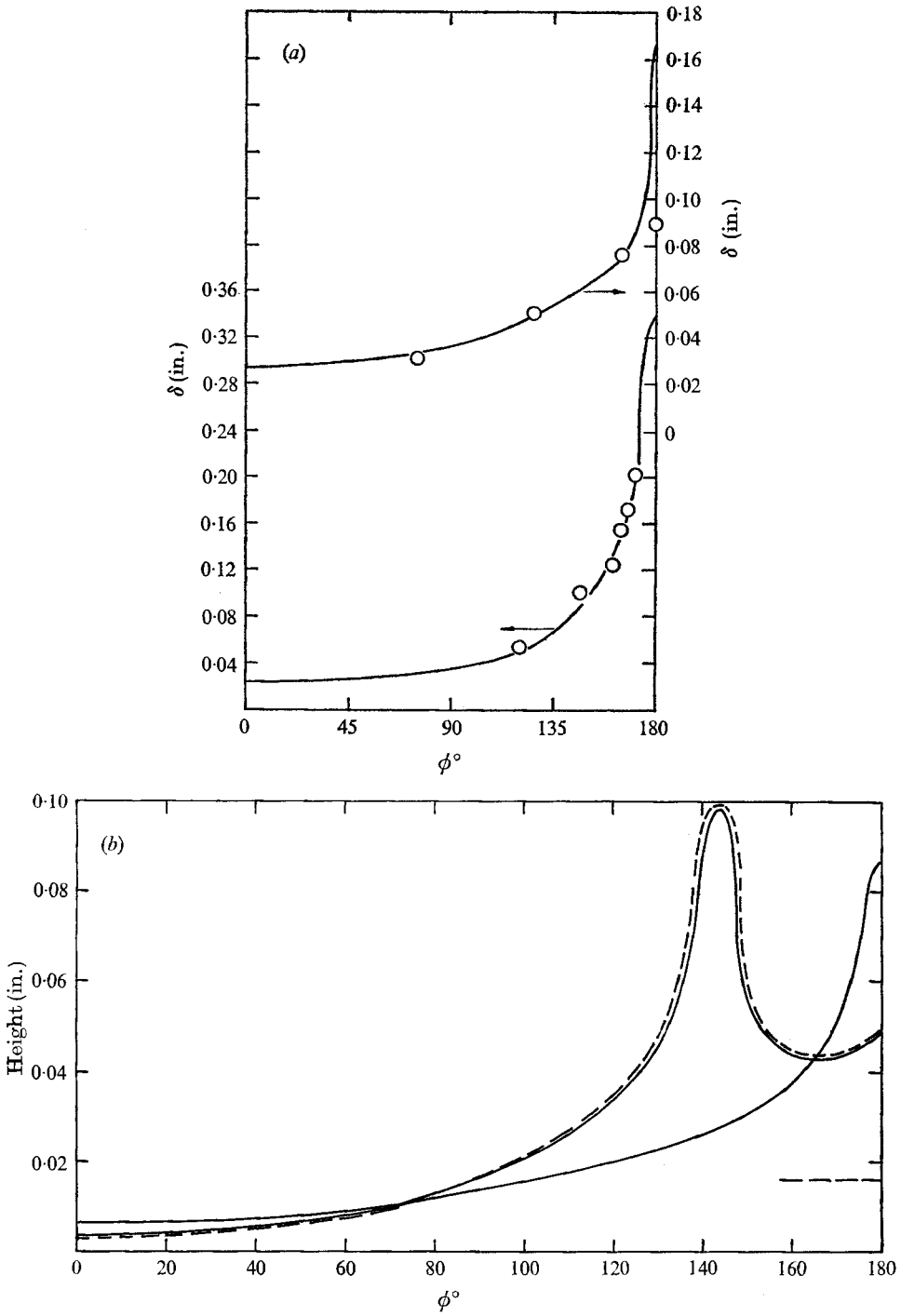

FIGURE 10. (*a*) Boundary-layer thickness. $M_\infty = 7{\cdot}95$, $T_w/T_0 = 0{\cdot}41$, $Rex = 3{\cdot}6 \times 10^5$. ○, experimental data (Tracy 1963); ——, present theory. (*b*) Displacement thickness. $M_\infty = 7{\cdot}95$; $\bar{x} = 1{\cdot}17$ in.; $Re = 1{\cdot}1 \times 10^5$. $\alpha = 20°$ (above): – – –, △; ——, δ_x^*. $\alpha = 8°$ (below): ——, △; – – –, axisymmetric δ_x^*.

the peak thickness locations off the symmetry plane are associated with two symmetric lobes containing the spiral vortices. Rainbird (1968) combined measurements of pitot pressure, surface static pressure and local flow inclination to obtain the velocity profiles and therefore δ_x. Our numerical results for displacement thickness are in qualitative agreement with Rainbird's experimental data, although his data were obtained at a much higher Reynolds number.

The variation of δ with angle of attack is depicted in figure 8(*b*). At the windward plane, the theoretical prediction almost coincides with the similar results of Reshotko (1957); at the leeward plane, the present theory indicates that both δ and Δ attain their maximum values at the onset of cross-flow reversal. They decrease at the lee side once the secondary-flow separation has been established. This type of variation in boundary-layer thickness has also been found by Poots (1965) for a three-dimensional compressible boundary layer at a point of attachment on a general curved surface.

It should be noted that the boundary-layer thickness near the leeward plane can be different from the so-called 'viscous-layer' thickness measured by Tracy (1963) and Marcillat (1970). This is due to the fact that the inviscid vortical singularity is diffused into a thin vortical layer, which is not a part of the boundary layer considered here (see, for example, George 1969; Yahalom 1971; Lin & Rubin 1972). In fact, the inner boundary of the vortical layer does not necessarily coincide with the outer edge of the boundary layer. Any interaction between these two regions has not been considered here.

6.3. *Cross-flow diffusion, local shear layers and resolutions*

All of the numerical results presented here include the influence of lateral diffusion (e.g. $u_{\phi\phi}$, etc.). To assess the importance of these effects, calculations have been performed with those terms neglected (i.e. $\epsilon = 0$ in (2.1)). For $\alpha = 2°$, as might be expected at this relatively small angle of incidence, there is little effect on the flow properties (figure 11), e.g. less than 3 % maximum change in heat transfer. However, at $\alpha = 12°$–$20°$, oscillations occur in the heat transfer and cross-flow velocity distributions, generally first appearing at an azimuthal location where cross-flow separation starts. These numerical wiggles grow as the integration proceeds downstream, until either the entire calculation is no longer meaningful or the computation becomes unstable. For $\alpha = 4°$–$8°$, the calculations also encounter instability, only this time at the lee plane. The boundary-layer thickness increases so rapidly at the leeward plane that crosswise diffusion becomes important as a shear layer forms.

The importance of choosing a refined grid near the separation line or boundary region is demonstrated in figure 9. At $\alpha = 4°$ with $\Delta\phi \leqslant 0{\cdot}2°$ near $\phi = 180°$, the difference in the solutions due to grid size are extremely small and $\delta \sim x^{0{\cdot}8}$; however, if $\Delta\phi = 2°$ near the leeward plane, $\delta \sim x^{1{\cdot}35}$ and significantly different profiles are found. Also shown is the boundary-layer thickness at several other locations. The results indicate that the boundary region is of the order 2° at $\alpha = 4°$.

When the separation line is off the leeward plane, specification of the grid becomes somewhat difficult. One can estimate the location of cross-flow separa-

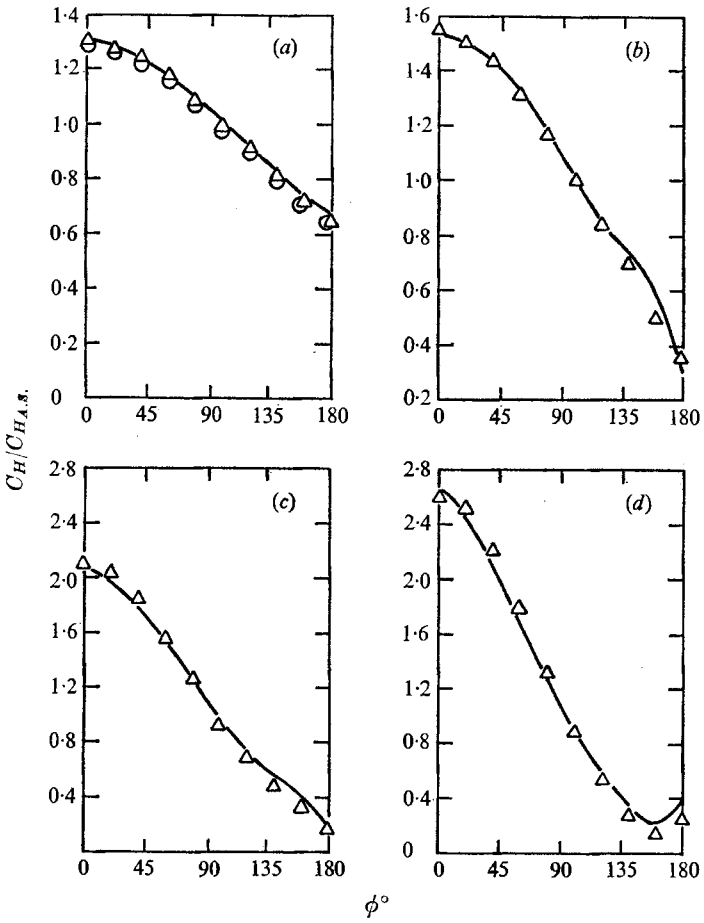

FIGURE 11. Heat transfer. $M_\infty = 7{\cdot}95$, $T_w/T_0 = 0{\cdot}41$. (*a*) $Rex = 4{\cdot}2 \times 10^5$, $\alpha = 2°$. ——, experimental data (Tracy 1963); △ (lateral diffusion), ○ (no lateral diffusion), present theory. (*b*) $Rex = 4{\cdot}2 \times 10^5$, $\alpha = 4°$. △, experimental data; ——, present theory. (*c*) $Rex = 4{\cdot}2 \times 10^5$, $\alpha = 8°$. (*d*) $Rex = 2{\cdot}1 \times 10^5$, $\alpha = 12°$.

tion or the so-called 'boundary region' by trial runs with a coarse grid and subsequent refinement in the separation region. We have found that with

$$\bar{r}\Delta\phi = O(\Delta\bar{y})$$

the results are quite acceptable.

From the windward plane to a location near the cross-flow separation line, the flow properties rapidly assume a similarity behaviour in all cases, and it is apparent that lateral diffusion is not significant outside the boundary region. A much larger grid size is possible for this portion of the flow field, and it is evident that once a similarity form has been achieved further integration is unnecessary. Therefore, if the boundary-layer solution in this region where similarity applies can be predetermined, the numerical calculation for the remainder of the flow from a point near the separation line to the leeward plane can be made separately. A finer grid can be specified so that adequate resolution

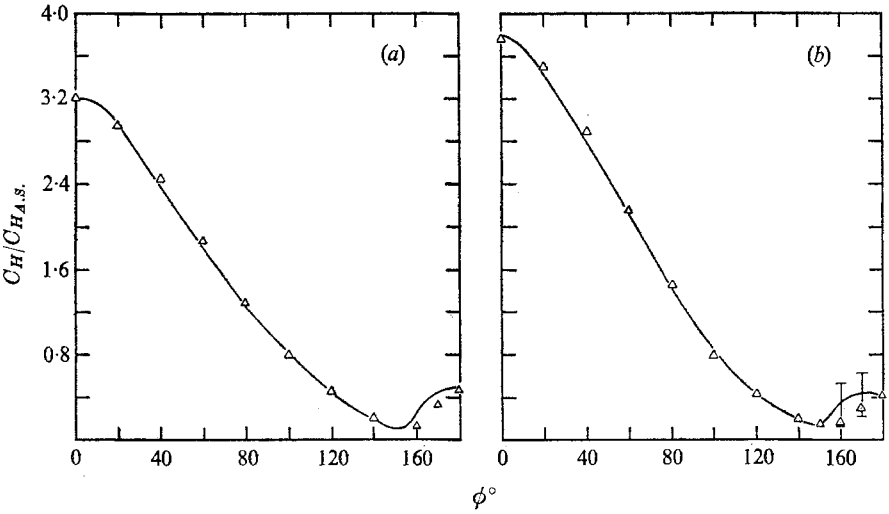

FIGURE 12. Heat transfer at large incidence. $M_\infty = 7{\cdot}95$, $T_w/T_0 = 0{\cdot}41$. $Re\,x = 2{\cdot}1 \times 10^5$. △, experimental data (Tracy 1963); ——, present theory; ⊥, temperature variation of 1 % in theory. α: (*a*) 16°; (*b*) 20°.

in the boundary region is recovered. This procedure is achieved by fixing the boundary conditions at some distance away from the separation line, with the predetermined similarity solutions instead of the windward symmetry conditions. This process can significantly reduce computer time, as well as computer storage. The similarity solution can be obtained either from the quasi-two-dimensional approach of Cooke (1966), Boericke (1971), Roux (1971), or by continuing the numerical marching technique presented herein until similarity is achieved. This technique has been extremely useful for obtaining accurate calculations of the flow in the boundary regions and near the leeward plane.

6.4. *Solutions*

(i) *Heat transfer.* Shown in figures 11 and 12 are the circumferential distribution of the heat transfer coefficient C_H for several angles of incidence. Here the Stanton number has been normalized with its axisymmetric value. The monotonic decrease in C_H, from the windward to the leeward generator, for angles of incidence $\alpha \leqslant 8°$, is typical of attached boundary-layer behaviour for a cone. For $\alpha > 8°$, a local minimum appears off the leeward plane. This is apparently due to the appearance of the pair of symmetric vortices associated with cross-flow separation. It is found that the location of minimum C_H does not exactly coincide with the secondary-flow separation point nor the position where the local static pressure is a minimum; however, the locations of these minimum values do not differ significantly.

Comparisons between the theoretical results and experimental data of Tracy (1963) are generally good, except near the leeward plane at the largest angle of attack, $\alpha = 20°$. This variance may be due to the fact that the local C_H values are quite small in this range, only 10 % of the axisymmetric value. Therefore,

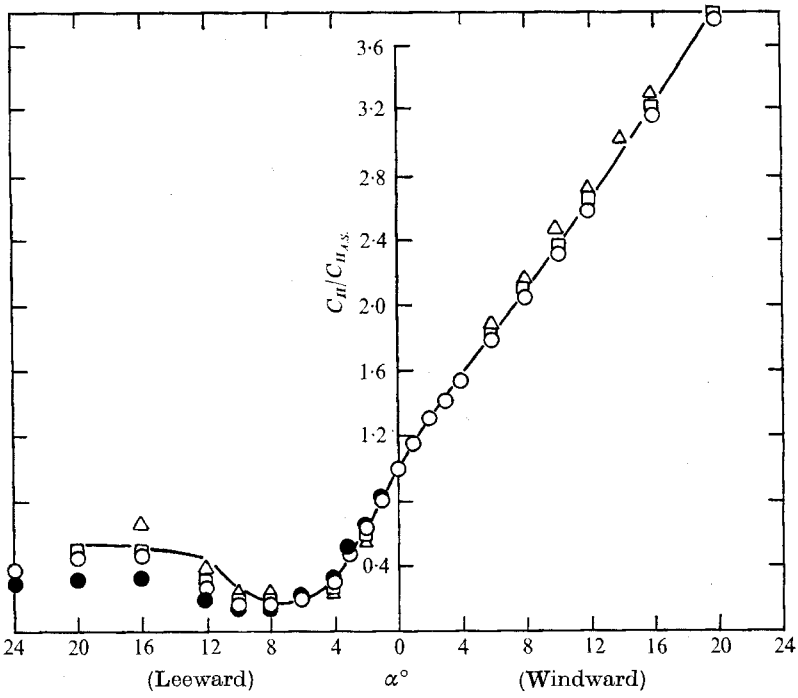

FIGURE 13. Heat transfer at symmetry plane. $Re\,x = 2{\cdot}1 \times 10^5 \ldots 7{\cdot}5 \times 10^5$, $\bar{x} = 3{\cdot}4$ in. ○, ●, □, △, experimental data (Tracey 1963); ——, present theory.

a 1 % error in the temperature near the surface could lead to a 50 % variation in the heat-transfer coefficient as determined from a temperature measurement or calculation (see figure 12). Unfortunately, Tracy does not discuss the scatter or accuracy of his experimental results in this region, presenting only a single data curve. Also, our calculated values for the temperature could easily be in error by 1 %. A summary of the Stanton number, for various angles of attack, at the leeward and windward planes is given in figure 13. C_H at the leeward plane initially decreases with increasing angle of attack, falling to a minimum at approximately the incidence angle corresponding to the onset of cross-flow reversal. C_H then begins to increase with further increases in α. A similar variation in the heat transfer is also observed by Poots (1965) in his study of a compressible three-dimensional boundary layer at a point of attachment. For the cone, agreement between the theoretical results and the experimental data at the symmetry planes is quite good for all angles of incidence.

In the streamwise direction the heat transfer exhibits parabolic decay (i.e. $C_H \sim x^{-\frac{1}{2}}$) at the windward side and generally in the region $\phi \leqslant 90°$. This behaviour is typical of the growth of a conventional boundary layer in the absence of any streamwise pressure gradient. Two distinct types of distribution are observed at the leeward plane of the cone. For $\alpha \leqslant 8°$, the heat-transfer coefficient decreases as $x^{-\frac{1}{2}}$, indicating a similarity behaviour once again. At angles of attack $\alpha > 8°$, C_H, as seen in figure 14, decreases less rapidly than $x^{-\frac{1}{2}}$. This trend is also apparent in Tracy's experimental data, where the leeward plane heat-

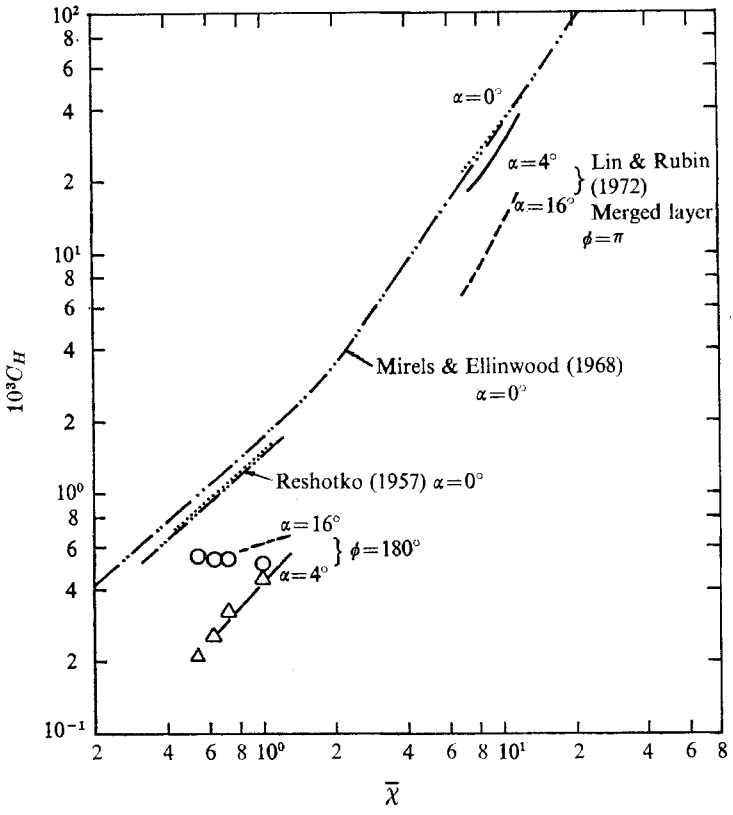

FIGURE 14. Variation of C_H with $\bar{\chi} = M_\infty^3 C^{\frac{1}{2}}/(Re\,x)^{\frac{1}{2}}$ at leeward plane. $M_\infty = 7{\cdot}95$, $T_w/T_0 = 0{\cdot}41$. Experimental data (Tracy 1963): △, $\alpha = 4°$; ○, 16. Present theory: – – –, $\alpha = 0°$; ——, 4; – – –, 16. $\phi = 180°$.

transfer coefficient remains almost invariant for a large range of Reynolds number at both $\alpha = 12°$ and 16°. Also shown on figure 14 is the theoretical heat-transfer distribution on a cone in the merged and strong interaction regions (Lin & Rubin 1972). Here, C_H tends to decrease with increasing Reynolds number as the cross-flow does not exhibit separation near the cone tip, and the vortex mixing process has not commenced.

(ii) *Boundary-layer profiles.* Typical profiles at a fixed streamwise location for the cross-flow velocities are shown in figure 15. There are significantly different characteristic profiles on the windward and leeward planes. On the windward side, the boundary layer is comparatively thin and gradients are quite large near the wall. On the leeward plane a much thicker layer with smaller surface shear is apparent.

On and near the windward plane, the flow profiles, as a function of streamwise distance, exhibit a similarity behaviour (figure 16). On the leeward plane, for $4° \leqslant \alpha < 10°$, the temperature distribution near the wall is still nearly similar, but the flow properties in the outer portion of the boundary layer are no longer of the similarity form (figure 16). For $\alpha \geqslant 10°$, the leeward boundary-layer thickness

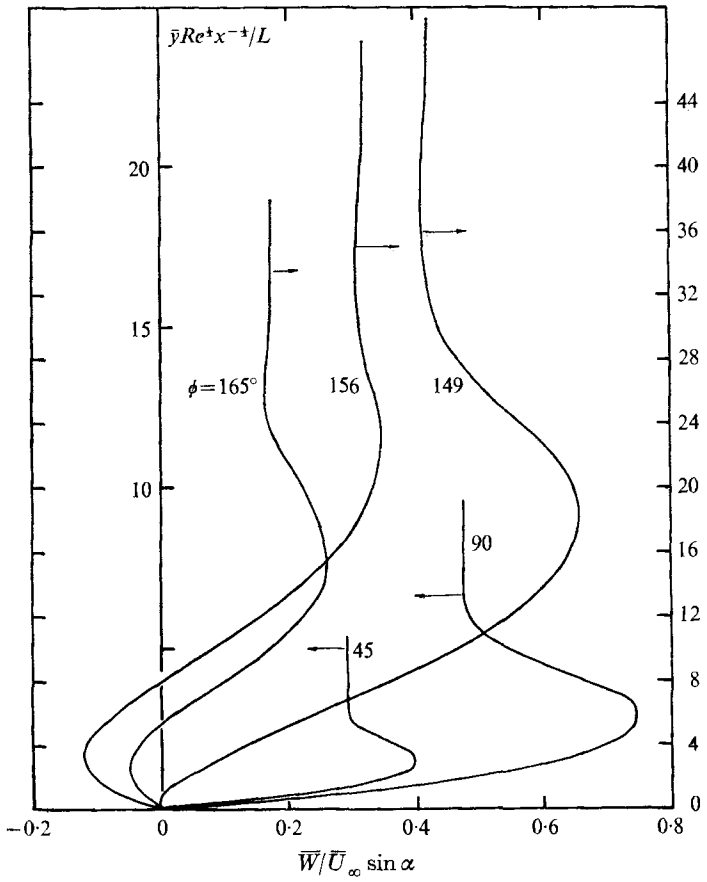

FIGURE 15. Flow profiles: azimuthal variations. $M_\infty = 7{\cdot}95$, $\theta = 10°$, $\alpha = 20°$, $T_w/T_0 = 0{\cdot}41$, $Re\,x = 2{\cdot}1 \times 10^6$.

returns to a near 'similarity' growth. These results reinforce our previous discussion concerning the failure of the similarity approximation for obtaining symmetry plane solutions for intermediate incidence angles.

(iii) *Effects of Mach number and surface temperature.* Variations in surface temperature appear to have little effect on the location of the cross-flow separation line (ϕ_s), although the inclination of the surface streamlines (upwash angle) increases monotonically with increasing wall temperature.

On the other hand, the distribution of azimuthal pressure gradient is significantly influenced by changes in the Mach number. For example, with $M_\infty = 2$, $\alpha = 8°$, $\theta = 10°$, the position of minimum local pressure, i.e. the position where the adverse p_ϕ is initiated, is at $\phi = 136°$ (Jones 1968). This location gradually moves toward the leeward plane with increasing M_∞, so that at $M_\infty = 20$ it is found at $\phi = 171°$. Since the location and extent of cross-flow separation are primarily determined by the distribution of the adverse azimuthal pressure gradient p_ϕ, the region of cross-flow as defined by the two swirling vortices is reduced when M_∞ is increased.

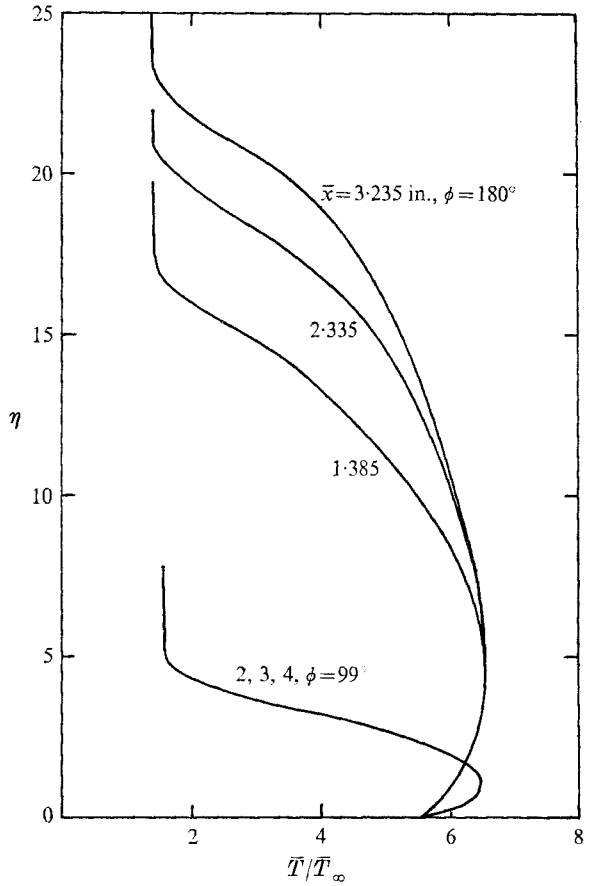

FIGURE 16. Flow profiles: streamwise variations. $M_\infty = 7{\cdot}95$, $\theta = 10°$, $\alpha = 4°$, $\beta = 0{\cdot}18$, $T_w/T_0 = 0{\cdot}41$.

Further discussion and results concerning the effects on the flow structure of grid size, M_∞, wall enthalpy, mass injection and centrifugal force (i.e. $p_y \neq 0$) are presented in an expanded version of the present paper (Lin & Rubin 1972).

7. Summary

A predictor–corrector, semi-implicit, finite-difference method has been developed to study the supersonic boundary layer on a slender cone at moderate angle of incidence ($\alpha/\theta \leqslant 2$). Comparisons have been made with available experimental data for heat transfer, pitot pressure, limiting streamline inclination and boundary-layer thickness. The agreement is generally good for all cases considered. The main conclusions of the analysis and numerical calculations are as follows.

(i) In a small region enclosing the cross-flow separation line, the boundary layer may exhibit a non-similar behaviour, thereby creating a boundary region with the lateral derivatives $[(1/r)(\partial/\partial\phi)]$ of the same order as the normal gradients $(\partial/\partial y)$.

(ii) A reduced mesh size must be specified to obtain adequate resolution of the flow structure inside the boundary region.

(iii) The cross-flow separation line is located at the leeward generator when $\alpha/\theta < 0{\cdot}8$, but moves away from the lee plane when cross-flow reversal occurs (e.g. with $\alpha = 20°$, $\theta = 10°$ and $M_\infty = 7{\cdot}95$, the separation streamline has moved to $\phi = \phi_s = 145°$).

(iv) The failure of Moore's similarity model at the leeward plane appears to be caused by local increased boundary-layer growth. The flow is no longer similar, and lateral diffusion (neglected in all previous symmetry plane analysis) must be retained, at least locally. Furthermore, non-similar behaviour at the lee surface has been shown to occur in the same range of the parameter

$$-0{\cdot}67 < K = \tfrac{2}{3}[\bar{w}_{e_\phi}/(\bar{u}_e \sin\theta)] < -0{\cdot}08$$

for which symmetry plane solutions have been unobtainable. When $K < -1$, solutions at the leeward plane exhibit a near similar behaviour; however, there is still small but non-zero streamwise variation in flow properties.

(v) Two helical vortices associated with cross-flow separation are created by an adverse azimuthal pressure gradient developing from opposing cross-flows. The vortices are maintained entirely within the boundary layer, and form downstream of the cone tip. The major portion of the vortex is moving at a supersonic speed.

(vi) Vortex interaction with the boundary layer leads to high localized heat transfer, and thinning of the boundary layer at the symmetry plane.

(vii) For favourable p_ϕ (i.e. lower angles of incidence) vortex formation and separation does not occur.

(viii) The wall cooling has a significant influence on the surface upwash. The hotter the wall, the larger the upwash angle.

(ix) As the free-stream Mach number increases, the region of cross-flow separation, if one exists, decreases. The swirling vortices are also reduced in extent with increasing M_∞.

This research is sponsored by the Air Force Office of Scientific Research, Office of Aerospace Research, USAF, under grant AFOSR 70-1843, project 9781-01.

REFERENCES

AVDUEVSKII, V. S. & MEDVEDEV, K. I. 1966 *Izv. AN SSR Mekhanika Zhidkosti i Gza.* 117–119.

BOERICKE, R. R. 1971 *A.I.A.A. J.* **9**, 462.

CHENG, H. K. 1961 *Cornell Aeronautical Lab. Rep.* AF-1285-A-3.

COOKE, J. C. 1966 *Royal Aeronautical Establishment TR* 66347.

DWYER, H. A. 1971 *A.I.A.A. Paper*, no. 71–57.

FELDHUN, R. 1971 *A.I.A.A. J.* **6**, 1074.

FLUGGE-LOTZ, I. & BLOTTNER, F. G. 1963 *J. de Mécanique*, **2**, 397.

GEORGE, O. L. 1969 *Sandia Labs., Albuquerque, N.M.*, SC-RR-69-577.

HALES, J. K. 1969 *Ordinary Differential Equations.* Wiley.

JONES, D. L. 1968 *National Research Council of Canada, Aero.* Rep. LR-507.

KRAUSE, E. 1967 *A.I.A.A. J.* **5**, 1231.

KRAUSE, E. 1969 *A.I.A.A. J.* **7**, 575.

KRAUSE, E., HIRSCHEL, E. H. & BOTHMANN, T. 1969 *A.I.A.A. J.* **2**, 367.

LIGHTHILL, M. J. 1958 *J. Fluid Mech.* **4**, 383.

LIN, T. C. & RUBIN, S. G. 1972 *Polytechnic Institute of Brooklyn, PIBAL Rep.* 72-27.

LIN, T. C. & RUBIN, S. G. 1973 *J. Computers & Fluids*, **1**, 37.

MCDEVITT, J. B. & MELLENTHIN, J. A. 1969 *N.A.S.A. Tech. Note*, D-5346.

MCGOWAN, J. J. & DAVIS, R. T. 1970 *Aerospace Research Labs. Rep.* ARL70-0341.

MARCILLAT, J. 1970 Thèse de Doctorat d'Etate, University of Provence, Marseille, France,

MASKELL, E. C. 1955 *Royal Aeronautical Establishment Aero. Rep.* 2565.

MIRELS, H. & ELLINWOOD, J. 1968 *A.I.A.A. J.* **6**, 2061.

MOORE, F. K. 1951 *N.A.C.A. Tech. Note*, no. 2279.

MOORE, F. K. 1953 *N.A.C.A. Tech. Rep.*, no. 1132.

MORETTI, G. 1967 *A.I.A.A. J.* **5**, 789.

MURDOCK, J. W. 1971 *The Aerospace Corp., San Bernardino, Calif., Air Force Rep.* SAMSO-TR-71-209.

POOTS, G. 1965 *J. Fluid Mech.* **22**, 197.

RAINBIRD, W. J. 1968 *A.I.A.A. J.* **6**, 2410.

RESHOTKO, E. 1957 *N.A.C.A. Tech. Note*, no. 4152.

ROUX, B. 1971 *J. de Mécanique*, **10**, 467.

RUBIN, S. G. 1972 *3rd Int. Symp. on Numerical Methods in Fluid Dynamics*, Paris. (Paper presented.)

RUBIN, S. G. & LIN, T. C. 1971 *Polytechnic Institute of Brooklyn, PIBAL Rep.* no. 71-8.

RUBIN, S. G. & LIN, T. C. 1972 *J. Comp. Phys.* **9**, 339.

STETSON, K. F. 1972 *A.I.A.A. J.* **10**, 642.

TRACY, R. R. 1963 *California Institute of Technology, Hypersonic Research Project Memo.* no. 69.

TRELLA, M. & LIBBY, P. A. 1965 *A.I.A.A. J.* **3**, 75.

VVEDENSKAYA, N. D. 1966 *USSR Computational Mathematics and Mathematical Physics*, **6**, 304.

WHITEHEAD, A. H. & BERTRAM, M. H. 1971 *A.I.A.A. J.* **9**, 1870.

YAHALOM, R. 1971 *University of California at Berkeley, Rep.* AS71-2.